RESEARCH ARTICLE
ATMOSPHERIC PHYSICS

Earth and Planetary Physics
10: 251–258, 2026
doi: 10.26464/epp2026025

Case analysis of diurnal stratospheric Rayleigh temperature and atmospheric fluctuations based on 589 nm lidar

ZhiFang Chen[1,2], ZhaoAi Yan[1,2*], Xiong Hu[1], WenJie Guo[1], ZunJie Wu[1,2], HaiLong Sun[1], ShangYong Guo[1], and YongQiang Cheng[1]

[1]State Key Laboratory of Solar Activity and Space Weather, National Space Science Center, Chinese Academy of Sciences, Beijing 100190, China;

[2]University of Chinese Academy of Sciences, Beijing 100049, China

Key Points:

- Gravity wave and tidal wave data were obtained by the first day–night lidar observations of the stratosphere in Yinchuan.
- The vertical wavelength and period of gravity waves detected in the range of 30–50 km were 8.53 km and 8.46 h.
- In the range of 30–34 km, the amplitudes of the diurnal tide and semi-diurnal tide were 0.6–2.5 K and 0.3–1.9 K.

Citation: Chen, Z. F., Yan, Z. A., Hu, X., Guo, W. J., Wu, Z. J., Sun, H. L., Guo, S. Y., and Cheng, Y. Q. (2026). Case analysis of diurnal stratospheric Rayleigh temperature and atmospheric fluctuations based on 589 nm lidar. *Earth Planet. Phys.*, *10*(2), 251–258. http://doi.org/10.26464/epp2026025

Abstract: Observational analysis of the Earth's stratospheric temperature structure and its dynamical behavior is of great significance for atmospheric dynamics research. In this paper, we present stratospheric temperatures in the range of 30–50 km above the Yinchuan observation site, retrieved from diurnal continuous Rayleigh scattering signal observation data collected by a 589 nm lidar throughout a single day. We also present observational studies of atmospheric tides and gravity wave cases. The diurnal temperature background field and perturbation field were obtained from the lidar data using the linear fitting method; these results exhibit good consistency with the temperature perturbation field extracted from ERA5. An obvious quasi-monochromatic inertial gravity wave was detected by application of a two-dimensional Fourier transform to the nighttime observation data with complete height coverage, which revealed these characteristic gravity wave parameters: a vertical wavelength of 8.53 km, a period of 8.46 h, and a downward-propagating vertical phase velocity. A nonlinear least-squares harmonic fitting method was used to extract amplitudes and phases of atmospheric diurnal and semi-diurnal tides in the 30–34 km range, where the diurnal data were relatively complete. The amplitudes increased with height, ranging from 0.6 to 2.5 K (diurnal tide) and 0.3 to 1.9 K (semi-diurnal tide), respectively. The phases showed a decreasing trend with height, indicating that the vertical phase velocity of the tides propagates downward while the energy propagates upward. These results indicate that diurnal 589 nm lidar observations data can provide important reference values for understanding the temperature structure of the stratosphere and the dynamical characteristics of atmospheric gravity waves and tides.

Keywords: stratosphere; atmospheric temperature; quasi-monochromatic inertial gravity wave; vertical wavelength; period; atmospheric tidal wave

1. Introduction

Rayleigh scattering lidar is an active remote-sensing optical technology that utilizes Rayleigh backscattering signals of atmospheric molecules excited by incident laser beams to measure the relative density and temperature of the atmosphere above 30 km. It has the advantages of enabling continuous observation and high temporal and range resolution, and has been widely applied in observational studies of the temperature structure and long-term trends of the middle atmosphere and characteristics of atmospheric waves (Guharay and Sekar, 2011; Llamedo et al., 2019; Guo WJ et al., 2020; Zhang RR et al., 2024; Li J et al., 2025). Due to the strength of competing solar scattered light during the daytime, the signal-to-noise ratio of echo signals from Rayleigh scattering lidar is greatly reduced, so most Rayleigh scattering lidars have operated primarily on clear nights. However, by developing ultra-narrowband filtering technology to suppress scattered solar light noise, previous investigators (Chen H et al., 1993, 1996) have shown that lidar can yield data useful in characterizing the middle atmosphere's entire diurnal thermodynamic structure and dynamical behavior. Lidar data have become an important new tool in middle atmosphere research.

For example, in 2015, G. Baumgarten et al. used a 532 nm lidar with an average power of approximately 15 W at the ALOMAR Observatory (69°N, 16°E), and realized daytime detection by utilizing a Fabry-Perot interferometer (FPI) with a full width at half maximum of 4.7 pm and an effective finesse of 25. They obtained

First author: Z. F. Chen, chenzhifang19@mails.ucas.ac.cn
Correspondence to: Z. A. Yan, yanza@nssc.ac.cn
Received 12 SEP 2025; Accepted 23 NOV 2025.
First Published online 30 DEC 2025.

approximately 50 hours of continuous day–night wind field and temperature data, and observed persistently active gravity wave phenomena; combined with wind speed, they used the Hodograph method to extract a vertical wavelength of approximately 5–10 km, with a period of 9.4 hours. The average momentum flux of quasi-monochromatic gravity waves within the range of 55–63 km was 3.8 m^2/s^2 (Baumgarten et al., 2015).

In 2017, K. Baumgarten et al. conducted gravity wave research using day–night observation data from the 532 nm lidar at Kühlungsborn (54°N, 12°E) collected from 2012 to 2015. This lidar achieved daytime detection by using an interference filter (with a bandwidth of 130 pm) and two FP etalons (with bandwidths of 4 pm and 4.5 pm, respectively). In this study, the authors adopted three processing methods: no filtering; vertical range filtering (<15 km); and temporal filtering (<8 h) that allowed separation of gravity waves from tidal waves. They found that the annual variation characteristics of potential energy density per unit mass differ under different filtering methods, demonstrating that the vertical wavelengths of gravity waves appear to be 8–12 km (using vertical range filtering <15 km) or 6–22 km (using temporal filtering <8 h) (Baumgarten et al., 2017). Based on the observed temperature data over ten days in 2016, they discovered that the amplitudes of 6–12-hour gravity waves and diurnal tides have a relationship: one increases while the other decreases. That inverse relationship suggests that gravity waves and tidal waves interact (Baumgarten et al., 2018). Chu et al. studied and realized daytime detection based on data from the Fe Boltzmann lidar at McMurdo (78°S, 167°E) using narrowband filters and FP etalons (Wang ZJ et al., 2012). In 2018, Zhao extracted the period (7.7 h) and vertical wavelength (10 km) of gravity waves over McMurdo from 66 hours of continuous observation data (Zhao J, 2018).

The National Space Science Center, Chinese Academy of Sciences (NSSC) has realized day–night detection of Rayleigh scattering echo signals on the basis of 589 nm sodium fluorescence Doppler lidar, using daytime detection technology based on a Sodium-vapor Faraday filter (Cheng XW et al., 2007).

In this paper, we retrieve atmospheric temperature data in the stratosphere (30–50 km) using Rayleigh scattering signals from the 589 nm lidar; we then extract and analyze case information describing atmospheric gravity waves and tidal waves. We present, for the first time, parameter characteristics of quasi-monochromatic gravity wave and tidal wave activities during day and night over Yinchuan (38.9°N, 105.8°E) in China. We suggest that such studies will enrich understanding of diurnal activities of atmospheric waves.

2. Data Sources and Analysis Methods

2.1 Data Sources

This paper is based mainly on 589 nm lidar Rayleigh scattering data and ERA5 reanalysis data. The former are used to retrieve the temperature profile over Yinchuan to understand the atmospheric wave conditions there. The ERA5 data reanalysis serves two purposes: it is used to establish the upper boundary of the lidar data used in the retrieval of atmospheric temperatures; it is used, also, to compare and verify the results of our analysis of lidar data with results obtained by other methods.

2.1.1 589 nm lidar Rayleigh scattering signal observation data

NSSC has been researching lidar detection technology since 2006; it has developed a 589 nm sodium fluorescence Doppler lidar and used this technology to conduct relevant scientific research (Ba J et al., 2017; Hu X et al., 2011). In 2023, NSSC developed a Rayleigh scattering signal day-and-night measurement technology based on a 589 nm lidar. The lidar's signal-receiving subsystem has been improved as follows: the lidar echo signals received by the telescopes are transmitted through a Sodium-vapor Faraday filter (as shown in the green solid border in Figure 1) to filter out the background light, and then to an iodine molecule absorption device (as shown in the red solid border in Figure 1). Daytime detection with the 589 nm lidar has been realized by inserting narrow-bandwidth interference filters in series with the Sodium-vapor Faraday filters. The narrow-bandwidth interference filter can filter out most of the solar background light. The Faraday filter consists of a high-temperature sodium vapor cell (as shown in the green dashed border in Figure 1) in a magnetic field, and two orthogonal polarizers. The principle of realizing daytime detection is as follows: the atmospheric echo signal becomes linearly polarized as it passes through the first polarizer (P1); together with the remaining solar background light, it then enters the sodium vapor cell. The narrow-band lidar echo resonates with the atomic transition energy level of the sodium vapor cell, and its polarization plane rotates by 90° (or an odd multiple thereof) under the appropriate magnetic field and temperature, allowing it to pass through the second polarizer (P2) smoothly. Most of the background light, however, has frequencies far from the resonant absorption line, so their polarization planes cannot rotate by 90° (or an odd multiple thereof); they cannot pass through the P2 (Cheng XW, 2006), which thus achieves the separation of the lidar echo light from the background light.

In order to achieve simultaneous measurement of wind and temperature, an iodine molecule absorption device is deployed in the signal receiving subsystem. A beam splitter (BS) is used to divide the echo signal into two channels, one of which is received directly by a photomultiplier tube (PMT1); this serves as the reference channel. The other channel passes its light through an I_2 vapor cell (as shown by the red dashed border in Figure 1) before being received by a photomultiplier tube (PMT2); this is the measurement channel. When performing temperature inversion, only reference channel signals are used.

The directions of outgoing laser beams are along 30° north off-zenith, 30° west off-zenith. The composition of this lidar system is shown in Figure 1 below, and the main parameters are listed in Table 1.

NSSC conducted a day–night continuous observation experiment using a 589 nm Doppler lidar in the area around Yinchuan on August 28, 2023, obtaining observation data lasting for one day. The temporal and range resolutions of data sampling were 6 s and 122.8 m, respectively. After filtering out abnormal data and data with excessively low signal-to-noise ratios, temporal and spatial accumulation was performed to improve the data signal-to-noise

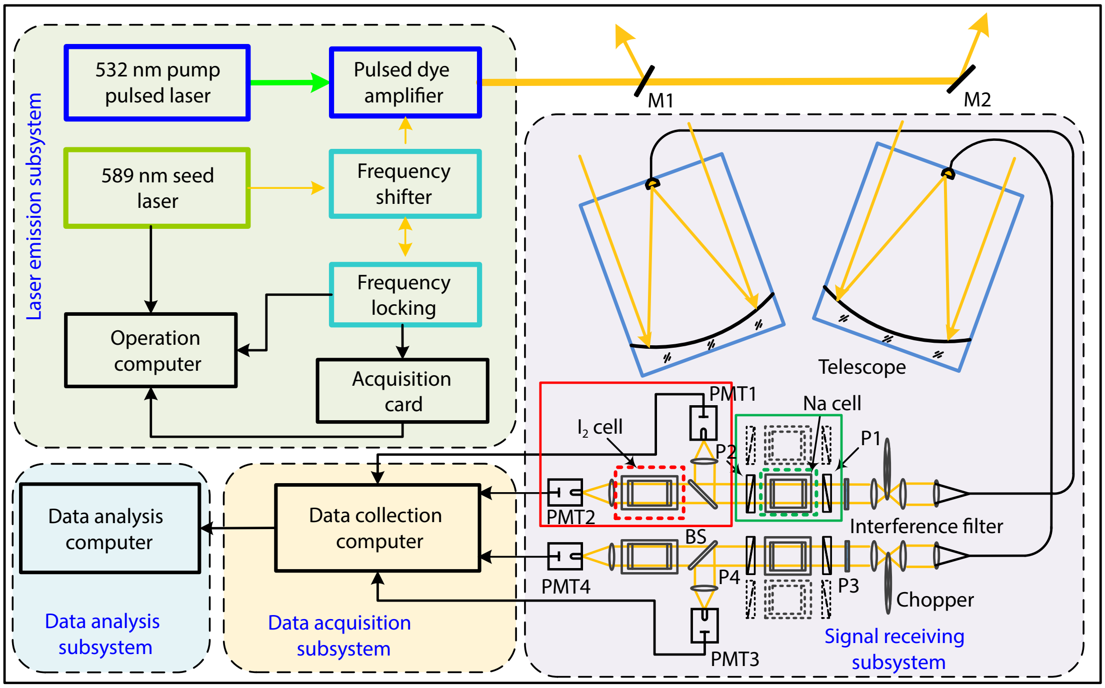

Figure 1. System of 589 nm Rayleigh scattering lidar. M1, M2: Mirror; P1–P4: Polarizer; BS: Beam Splitter; PMT1–PMT4: Photomutiplier Tube.

Table 1. Main parameters of the 589 nm Rayleigh scattering lidar.

Parameters	Value
Wavelength	589.158 nm
Pulse duration	10 ns
Pulse repetition frequency	100 Hz
Laser power	1.2 W
Telescope diameter	1 m
Filter band	0.5 nm
PMT quantum efficiency	15%
Temporal resolution	1 hour
Height resolution	1 km

ratio. Finally, 23 echo photon profiles with detection heights above 30 km and temporal and height resolutions of 1 hour and 1 km were obtained.

2.1.2 ERA5 reanalysis data

The ERA5 reanalysis data is the fifth-generation global climate reanalysis dataset developed by the European Centre for Medium-Range Weather Forecasts (ECMWF), evolved from the ERA-Interim reanalysis dataset (Hersbach et al., 2020). ERA5 datasets combine model data with observational data, providing high-resolution climate data from 1950 to the present. This paper analyses data on geometric height, atmospheric density, and atmospheric temperature for August 23, 2023, taken from the Complete ERA5 global atmospheric reanalysis (https://cds.climate.copernicus.eu/datasets/reanalysis-era5-complete?tab=d_download), which provides hourly data of various atmospheric parameters on a global scale. Since the data published by ERA5 is gridded (0.25° × 0.25°), average values of data from the four grid points closest to the longitude and latitude of the test site (38.75°N, 105.9°E; 38.75°N, 105.75°E; 39°N, 105.75°E; 39°N, 105.9°E) are used for the following analysis.

2.2 Analysis Methods

2.2.1 Rayleigh temperature retrieval method

The research in this paper uses Rayleigh scattering signals from a 589 nm Rayleigh scattering Doppler lidar to retrieve temperatures in the range of 30–50 km and to extract evidence of gravity waves. During preprocessing, signals with low signal-to-noise ratios and other abnormal data are first removed; the data considered valid are then accumulated and smoothed, and background noise is minimized. The strength of the 589 nm Rayleigh scattering Doppler lidar echo signals shows an exponentially decreasing trend with height; combined with the low power of the lidar, this means that the measurement uncertainty at higher altitudes is significantly greater than that at lower altitudes. To increase the height of reliable echo data and to reduce the uncertainty of atmospheric temperature retrieval, echo signals of the three frequencies in the reference channel are accumulated for 1 hour, smoothed using a 2 km Hanning window, and then used to retrieve the temperature profile $T(z)$ according to the Chanin-Hauchecorne method (CH method) (Hauchecorne and Chanin, 1980):

$$T(z) = \frac{n_{zu}T_{zu} + \frac{1}{R_d}\int_{z}^{zu} n(z_i)\,g\mathrm{d}z_i}{n(z)}. \tag{1}$$

Here, z is height, zu is the upper boundary height. Density and temperature at the upper boundary are represented by n_{zu} and T_{zu}, respectively, which can usually be obtained from models (the upper boundary density and temperature data in this paper are derived from ERA5 reanalysis data). R_d is the gas constant for dry air, g is the gravitational acceleration, and $n(z)$ is the density profile.

2.2.2 Method for extracting temperature background field and temperature disturbance

According to the linear theory of gravity waves, the atmospheric temperature field $T(z,t)$ can be considered as consisting of the background temperature field $\overline{T}(z,t)$ and the temperature perturbation field $T'(z,t)$ caused by gravity waves. Therefore, the premise for analyzing the characteristics and propagation properties of gravity waves is to extract temperature perturbations from the atmospheric temperature, which requires first determining the background temperature field of the atmosphere. Of the various methods to determine the background temperature field, the method adopted in this paper is as follows:

Temperature data are screened; data with uncertainty greater than 10 K are excluded; inversion results are retained only if they exhibit a relatively high signal-to-noise ratio.

A linear fit is performed along the time direction at each altitude to obtain the background temperature field $\overline{T}(z,t)$, with a height resolution of 0.1 km and a temporal resolution of 1 hour.

The initial temperature perturbation field is obtained by subtracting the background temperature from the measured temperature. Then a 5th-order Butterworth band-pass filter is used to filter out the effects of waves with vertical wavelengths less than 2 km and greater than 15 km, resulting in temperature perturbations assumed to be caused mainly by atmospheric gravity waves.

$$T'(z,t) = T(z,t) - \overline{T}(z,t). \tag{2}$$

The temperature perturbations extracted by this method can capture the characteristics of gravity waves with periods less than 24 hours. Subtracting the background temperature field removes time-varying trends in atmospheric temperature, effectively eliminating the influences of long-period tidal waves, planetary waves, and gravity waves whose periods exceed the duration of the observational period being analyzed.

2.2.3 Two-dimensional fourier spectral method for temperature perturbation field

To obtain vertical wavelengths and periods of gravity waves, Formula (3), a two-dimensional Fourier transform (using the FFT2 function in Matlab), is applied to process the temperature perturbation field. According to traditional spectral analysis methods, zeros are padded to the sampling points in both the time and range series, making the number of sampling points 1024 for each. Then a two-dimensional fast Fourier transform is performed on the temperature disturbance, with the specific formula as follows:

$$Y_{p+1,q+1} = \sum_{j=0}^{n_1-1}\sum_{k=0}^{n_2-1} \omega_{n_1}^{jp}\omega_{n_2}^{kq} X_{j+1,k+1}. \tag{3}$$

Here, n_1 and n_2 represent the number of rows and columns of the input matrix $\boldsymbol{X}$; i.e., $T'(z,t)$ corresponds to the number of points of the perturbation field in range and time; thus Y is the result of the two-dimensional Fourier transform, representing the amplitude spectrum of gravity waves. Substituting the complex roots of unity $\omega_{n_1} = \mathrm{e}^{-2\pi \mathrm{i}/n_1}$ and $\omega_{n_2} = \mathrm{e}^{-2\pi \mathrm{i}/n_2}$ into the formula, it can be rewritten as

$$Y_{p+1,q+1} = \sum_{j=0}^{n_1-1}\sum_{k=0}^{n_2-1} \mathrm{e}^{-\mathrm{i}(2\pi jp/n_1+2\pi kq/n_2)} X_{j+1,k+1}. \tag{4}$$

When analyzing the propagation direction and phase of waves, the wave equation is expressed in complex form as follows:

$$T(z,t) = A\mathrm{e}^{\left[\mathrm{i}(\omega-m-\varphi)+\frac{z}{2H}\right]}, \tag{5}$$

A is the amplitude of the wave, ω is the angular frequency, m is the vertical wave number, and φ is the initial phase, H is density scale height. In this case, when ω and m have the same sign, the wave propagates upward; when they have opposite signs, the wave propagates downward. By comparing Formulae (4) and (5), $\omega = 2\pi q, m = -2\pi p$. The symbols used for the spatial terms ($2\pi jp/n_1$ and $-mz$) in the Formulae (4) and (5) are opposite. By multiplying the spatial frequency axis of the two-dimensional Fourier transform result by −1, $p'(-p)$ and $m = 2\pi p'$ were obtained, which is convenient for subsequent analysis.

2.2.4 Tidal extraction method

To extract the tides, we adopt the nonlinear least-squares harmonic fitting method (using the lsqcurvefit function in Matlab), which can fit the amplitude and phase of tides and realize the extraction of tidal components that exhibit different periods. When it is necessary to extract diurnal tides and semi-diurnal tides, the basic formula of harmonic fitting can be written as

$$T(t) = \overline{T}(t) + A_{24}\cos\left(\frac{2\pi}{24}t - \varphi_{24}\right) + A_{12}\cos\left(\frac{2\pi}{12}t - \varphi_{12}\right), \tag{6}$$

where $T(t)$ represents a time-varying sequence at a specific altitude; $\overline{T}(t)$ denotes the background temperature, which has a linear correlation with time; A_{24} and A_{12} stand for the amplitudes of the diurnal and semi-diurnal tides, respectively; φ_{24} and φ_{12} refer to the corresponding phases, indicating the times when the amplitudes reach their maximae.

3. Results and Discussion

3.1 Diurnal Temperature Structure

Diurnal temperatures retrieved using the CH method are shown in Figure 2, which presents the temperature contour map obtained from the lidar data from 00:00 to 23:00 (UT) on August 28, 2023; the abscissa represents time, the ordinate represents altitude. Due to signal-to-noise ratio limitations, only the echo signals at night, dawn, and dusk can be used to retrieve reliable atmospheric temperatures in the 30–50 km range. Although the daytime detection altitude is somewhat reduced, an acceptable overall temperature structure can be approximated. Atmospheric temperature increases with altitude, which is characteristic of the stratospheric temperature structure.

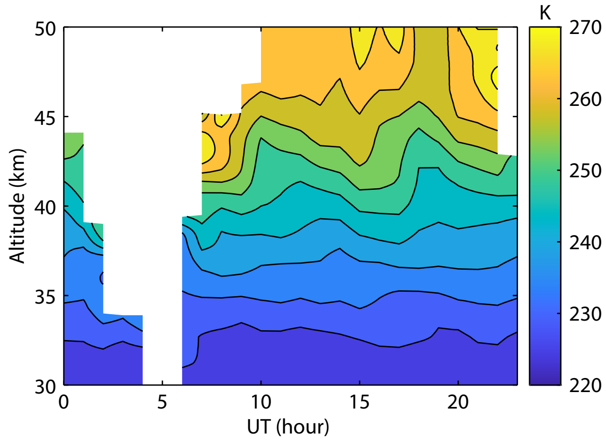

Figure 2. Temperature detected by the 589 nm lidar from 00:00 to 23:00 (UT) on August 28, 2023.

According to detection results of the lidar shown in Figure 2, stratospheric temperature, apart from increasing with altitude, exhibits an obvious wavelike structure in its diurnal variations. The temperature changes are caused mainly by ozone absorption of solar ultraviolet radiation; the wavelike vertical structure is thought to be a consequence of the dynamic behavior of atmospheric waves. As altitude increases, the amplitudes of temperature fluctuations become larger with time (UT).

3.2 Diurnal Temperature Perturbations

Figure 3, below, presents further detail regarding the atmospheric waves retrieved from data collected on August 28, 2023. These additional details were made possible by comparing temperature perturbations extracted from the temperature profiles based on that day's lidar data with temperature perturbations extracted from the ERA5 reanalysis data using the same method. Figure 3a shows the temperature perturbations detected by the lidar from 00:00 to 23:00 (UT) on August 28, 2023, while Figure 3b shows the temperature perturbations extracted from the ERA5 reanalysis data at the corresponding grid locations and times. The abscissa represents time, the ordinate represents altitude. It can be observed that both temperature perturbations exhibit obvious and similar wavelike structures in atmospheric temperature perturbations. Although there are certain data gaps during the daytime, the overall structure of temperature perturbations detected by the lidar indicates signs of gravity wave activity during both the day and the night, which is somewhat consistent with the temperature perturbation structure extracted from the reanalysis data.

The crests of gravity waves are marked with auxiliary lines (red straight lines); note that the positions of the red auxiliary lines in both Figures 3a and 3b are the same. The missing parts of the lidar detection data are indicated by dashed lines. The auxiliary lines slope downward to the right, indicating that the gravity waves active on that day had downward-propagating phases; the distances between the wave crests are similar, so they can be regarded as quasi-monochromatic gravity waves.

3.3 Characteristic Parameters of Monochromatic Gravity Waves

Since the nighttime data quality is better and the altitude coverage is more complete, the temperature perturbations from 10:00 UT to 21:00 UT on that day were extracted separately to observe the nighttime gravity wave structure. Figure 4a shows the temperature perturbations detected by the lidar during this period, and Figure 4b shows those from ERA5. Overall, gravity wave amplitudes increase with altitude; nighttime lidar observations are closely similar to those from the ERA5 reanalysis data.

To obtain accurately the vertical wavelength and period of the gravity wave activity that night, a two-dimensional fast Fourier transform was performed on the temperature perturbations, in both time and space domains, to derive the amplitude spectrum. Due to the symmetry of the discrete Fourier transform, only the results of the right half (with positive frequencies) are retained, as shown in Figure 5. The abscissa represents frequency, which is the reciprocal of the period; the ordinate represents vertical wavenumber, which is the reciprocal of the vertical wavelength. The period and vertical wavelength of the dominant gravity wave activity that night can be obtained from the data corresponding to the peak of the amplitude spectrum with confidence level greater than 95%: specifically, a vertical wavelength of 8.53 km, and a period of 8.46 h. According to Equation (5), the propagation

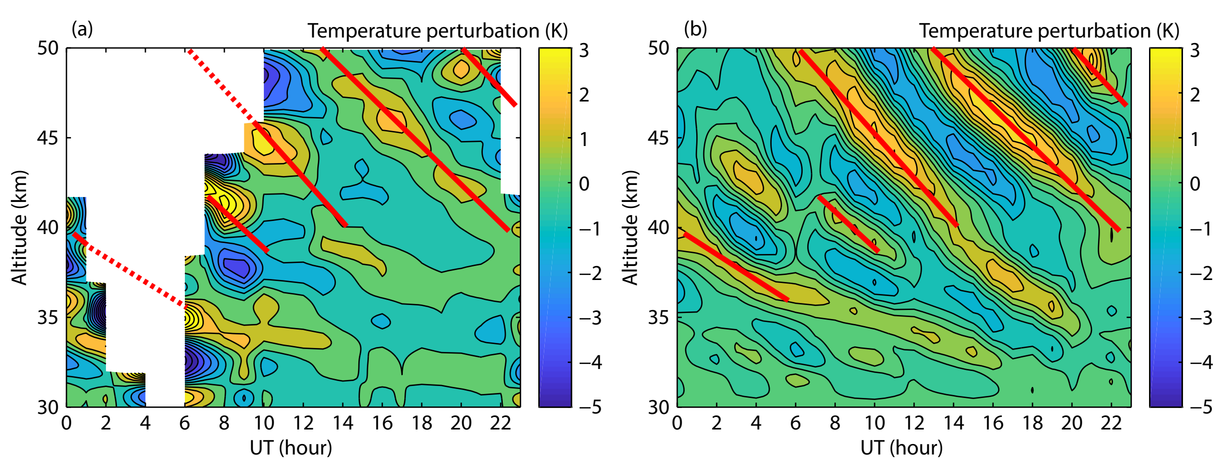

Figure 3. Temperature perturbations from 00:00 to 23:00 (UT) on August 28, 2023. (a) Lidar data; (b) ERA5 reanalysis data.

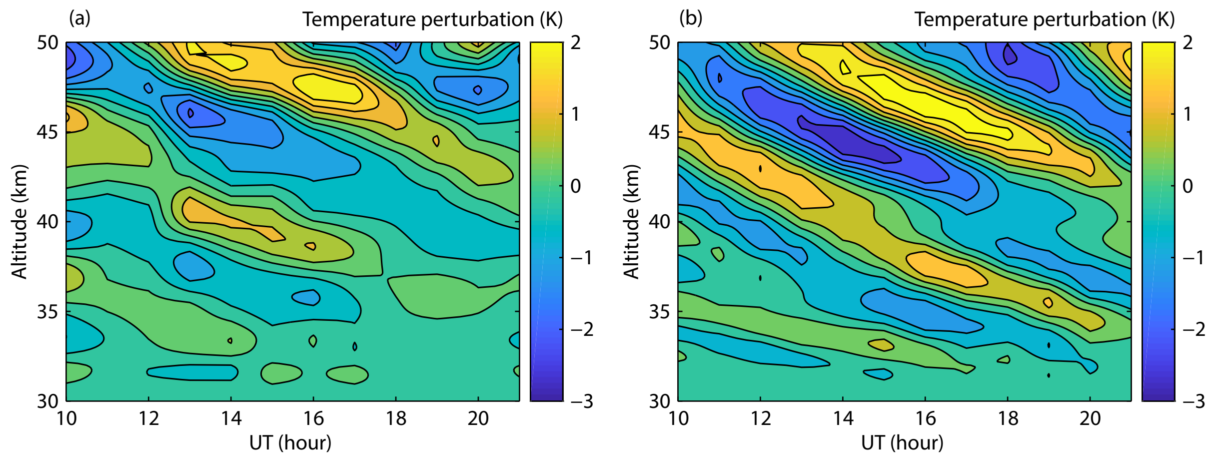

Figure 4. Temperature perturbations from 10:00 to 21:00 (UT) on August 28, 2023. (a) Lidar data; (b) ERA5 reanalysis data.

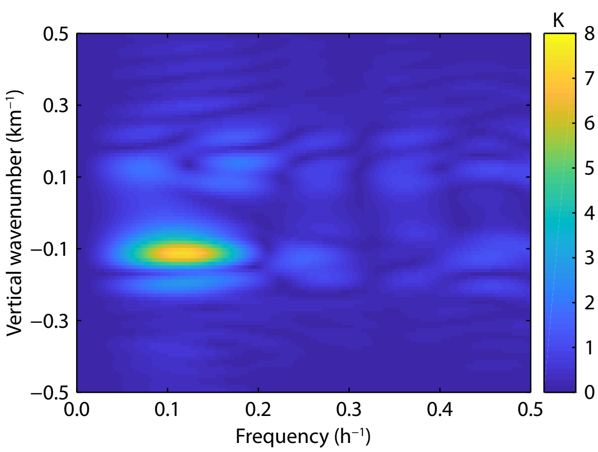

Figure 5. Amplitude spectrum of temperature perturbations from lidar detection data on August 28, 2023.

direction of the gravity wave is determined by the signs of both ω and m. As shown in Figure 5, $\omega/m < 0$, indicating that the phase of the gravity wave propagated downward that night.

3.4 Comparison with Other Observation Sites

In numerous studies of stratospheric gravity waves, the ranges of their vertical wavelengths have been as follows: 5–9 km, for gravity waves observed over low-latitude Haikou (20.0°N, 110.3°E) (Gong SH et al., 2023); 1.1–17 km, for waves observed at low-latitude Arecibo Observatory (18°N, 67°W) (Beatty et al., 1992); from 4 to 14 km, in mid-latitude regions, with latitudes close to that of the experimental site in this paper, from lidar observation data in Xinzhou (38.4°N, 112.7°E) and Jiuquan (39.7°N, 98.5°E) (Zhao RC et al., 2016). The vertical wavelengths of stratospheric gravity waves measured over Illinois, USA (40°N, 88°W) are 2–11.5 km (Gardner et al., 1989); thus the 8.53 km wavelength of the gravity wave observed in this paper is consistent with this range. In high-latitude regions, the vertical wavelengths observed at McMurdo (77.84°S, 166.69°E) in winter and summer are 8 km and 5.5 km, respectively (Zhao J, 2018).

These observational results have revealed that vertical wavelengths of stratospheric gravity waves can vary within latitudinal regions, perhaps reflecting different geographical features. For example, in U. Blum's research, simultaneous lidar observations at two locations just 250 km apart but on either side of a mountain showed that the observed gravity waves were similar in potential energy density per unit volume, but significantly different in their vertical wavelengths (1–12 km vs. 2–6 km) (Blum et al., 2004), suggesting that gravity wave activities are affected by factors such as topography. Analysis of significantly increased observational data, gathered in a wider range of situations, can be expected to result in rapid advances in our understanding of gravity wave patterns. .

3.5 Extraction of Amplitudes and Phases of Diurnal and Semi-diurnal Tides

In addition to gravity waves, tides are an important atmospheric wave component, of which diurnal and semi-diurnal tides dominate. In this paper, the least-squares harmonic fitting method is used to study tidal activities in the 30–34 km range where currently available data coverage and accuracy are relatively good. The extracted amplitudes and phases of diurnal and semi-diurnal tides are shown in Figure 6 below; in Figure 6a, the solid and dotted line represent the amplitudes of diurnal and semi-diurnal tides, respectively, with standard errors indicated by error bars. Figure 6a shows that within the 30–34 km range, the amplitude of the diurnal tide is slightly larger than that of the semi-diurnal tide, and overall, the tidal amplitudes increase with increasing altitude. The variation ranges of the amplitudes of diurnal and semi-diurnal tides within the 30–34 km range are 0.6–2.5 K and 0.3–1.9 K, respectively.

Figure 6b illustrates the trend of diurnal tide (solid line) and semi-diurnal tide (dotted line) phase variation with height. As shown in the figure, these phases generally exhibit a decreasing trend with height, indicating that the propagation direction of tidal phases is downward. Tides are generally considered to be caused primarily by the absorption of heat from solar radiation and from latent heat release in the lower atmosphere, including infrared radiation from the sun absorbed by water vapor in the troposphere and ultraviolet radiation from the sun absorbed by stratospheric

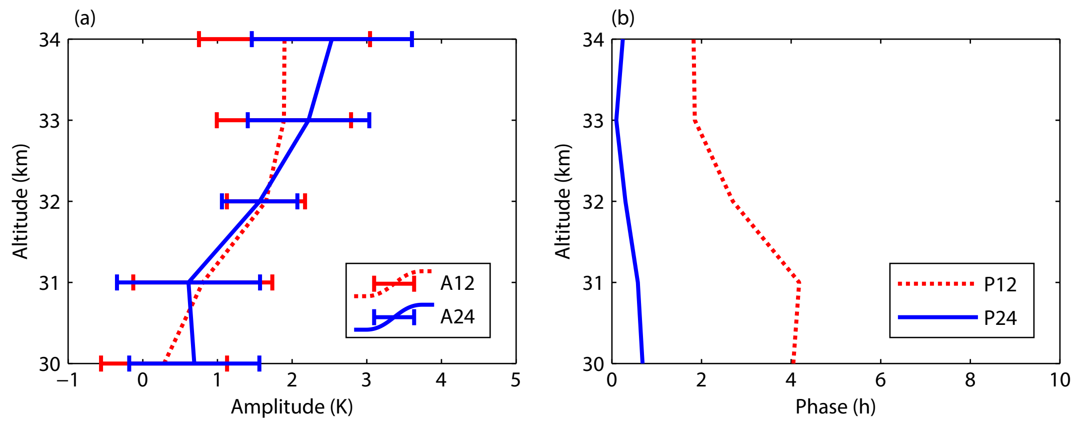

Figure 6. (a) Amplitudes and (b) phases extracted from lidar temperature data on August 28, 2023. A12: Semidiurnal tidal amplitude; A24: Diurnal tidal amplitude; P12: Semidiurnal tidal phase; P24: Diurnal tidal phase.

ozone (Chapman and Lindzen, 1970). During the upward propagation of tides, the amplitude increases with height, while the direction of phase propagation is downward. The research results presented in this paper align with this basic law.

The amplitudes of diurnal and semi-diurnal tides extracted from temperature data obtained by lidar (54°N, 12°E) (Baumgarten et al., 2018) and radio occultation (10°S–10°N) (Xie F et al., 2010) both fall within the range of 0–1 K, which is slightly smaller than the amplitude range in Figure 6a but within the error range. The tidal amplitudes obtained by ground-based temperature radiometer (Krochin et al., 2024) in the central area of the Northern Hemisphere (46.95°N, 7.45°E; 46.82°N, 6.94°E) are 1.5–2.8 K (diurnal tide) and 1–1.7 K (semi-diurnal tide) respectively, which are comparable to results in this paper.

4. Conclusions

Based on one day of observational data obtained from a 589 nm Rayleigh scattering lidar in the Yinchuan area, this paper presents, for the first time, a diurnal atmospheric temperature structure, the characteristics of an atmospheric gravity wave, and diurnal/semi-diurnal tidal wave activities in the stratospheric range of 30–50 km over Yinchuan, which are summarized as follows:

(1) The stratospheric temperature increases with altitude, superimposed with atmospheric wave phenomena; these features are roughly similar to those from ERA5 temperature data;

(2) Analysis of the observed nighttime quasi-monochromatic atmospheric gravity wave reveals that its vertical wavelength was 8.53 km and its period was 8.46 h, which are similar to ERA5 reanalysis data and to the atmospheric gravity wave parameters of other stations at similar latitudes, but different from observation results obtained at different latitudes;

(3) In the altitude range of 30–34 km, the amplitude of the diurnal tide observed in this study was 0.6–2.5 K, and that of the semi-diurnal tide was 0.3–1.9 K. Their phases both propagated downward, which is consistent with tidal results obtained from other types of data, but the values reported here are slightly different.

The results above demonstrate the potential of 589 nm lidar to enrich our understanding of stratospheric atmospheric temperature and wave characteristics. Of course, considerably more observational data will be needed to analyze and statistically study the dynamic behavioral characteristics of the stratospheric atmosphere. Also by increasing data integration times and altitude resolution (2 hours, 2 km), echo data from 532 nm lidars with higher transmission power (usually over 10 W), and equipped with a 1.8 m diameter receiving telescope, can be detected from altitudes as great as 80 km even during the daytime (Baumgarten et al., 2015). The iron Boltzmann lidar (372 nm, 374 nm) has not only high transmission power but also a larger Rayleigh scattering cross-section, enabling daytime detection up to 70 km with range and temporal resolutions of 1 km and 1 hour, respectively (Chen C et al., 2016). Thus, future studies of this sort should be able to achieve improved structural detail. In conclusion, we suggest that diurnal Rayleigh temperature data from the 589 nm lidar will be of great value in future research on the variation characteristics of the stratosphere.

Acknowledgments

This study was supported by the Key Research Program of the Chinese Academy of Sciences (Grant NO. KGFZD-145-23-17) and the Specialized Research Fund for State Key Laboratories. We also acknowledge the use of the ERA5 reanalysis data from the European Centre for Medium-Range Weather Forecasts; relevant data can be accessed from https://cds.climate.copernicus.eu/datasets/reanalysis-era5-complete?tab=d_download.

References

Ba, J., Hu, X., Yan, Z. A., Guo, S. Y., and Cheng, Y. Q. (2017). Lidar observations of atmospheric gravity wave dissipation induced Na atoms transportations in the mesopause region at Langfang, China. *Chinese J. Geophys. (in Chinese)*, *60*(2), 499–506. https://doi.org/10.6038/cjg20170205

Baumgarten, G., Fiedler, J., Hildebrand, J., and Lübken, F. J. (2015). Inertia gravity wave in the stratosphere and mesosphere observed by Doppler wind and temperature lidar. *Geophys. Res. Lett.*, *42*(24), 10929–10936. https://doi.org/10.1002/2015GL066991

Baumgarten, K., Gerding, M., and Lübken, F. J. (2017). Seasonal variation of gravity wave parameters using different filter methods with daylight lidar measurements at midlatitudes. *J. Geophys. Res.: Atmos.*, *122*(5), 2683–2695.

https://doi.org/10.1002/2016JD025916

Baumgarten, K., Gerding, M., Baumgarten, G., and Lübken, F. J. (2018). Temporal variability of tidal and gravity waves during a record long 10-day continuous lidar sounding. *Atmos. Chem. Phys.*, *18*(1), 371–384. https://doi.org/10.5194/acp-18-371-2018

Beatty, T. J., Hostetler, C. A., and Gardner, C. S. (1992). Lidar observations of gravity waves and their spectra near the mesopause and stratopause at Arecibo. *J. Atmos. Sci.*, *49*(6), 477–496. https://doi.org/10.1175/1520-0469(1992)049<0477:LOOGWA>2.0.CO;2

Blum, U., Fricke, K. H., Baumgarten, G., and Schöch, A. (2004). Simultaneous lidar observations of temperatures and waves in the polar middle atmosphere on the east and west side of the Scandinavian mountains: A case study on 19/20 January 2003. *Atmos. Chem. Phys.*, *4*(3), 809–816. https://doi.org/10.5194/acp-4-809-2004

Chapman, S., and Lindzen, R. S. (1970). *Atmospheric Tides: Thermal and Gravitational*. Dordrecht: Springer. https://doi.org/10.1007/978-94-010-3399-2

Chen, C., Chu, X. Z., Zhao, J., Roberts, B. R., Yu, Z. B., Fong, W., Lu, X., and Smith, J. A. (2016). Lidar observations of persistent gravity waves with periods of 3−10 h in the Antarctic middle and upper atmosphere at McMurdo (77.83°S, 166.67°E). *J. Geophys. Res.: Space Phys.*, *121*(2), 1483–1502. https://doi.org/10.1002/2015JA022127

Chen, H., She, C. Y., Searcy, P., and Korevaar, E. (1993). Sodium-vapor dispersive Faraday filter. *Opt. Lett.*, *18*(12), 1019–1021. https://doi.org/10.1364/OL.18.001019

Chen, H., White, M. A., Krueger, D. A., and She, C. Y. (1996). Daytime mesopause temperature measurements with a sodium-vapor dispersive faraday filter in a lidar receiver. *Opt. Lett.*, *21*(15), 1093–1095. https://doi.org/10.1364/OL.21.001093

Cheng, X. W. (2006). Technologies of dual-wavelength high altitude lidar and daytime observation for Na channel [Master thesis] (in Chinese). Wuhan: Wuhan Institute of Physics and Mathematica, Chinese Academy of Science.

Cheng, X. W., Gong, S. S., Li, F. Q., Dai, Y., Song, J., Wang, J. M., and Li, F. Y. (2007). 24 h continuous observation of sodium layer over Wuhan by lidar. *Sci. China Ser. G: Phys. Mech. Astron.*, *50*(3), 287–293. https://doi.org/10.1007/s11433-007-0032-z

Gardner, C. S., Miller, M. S., and Liu, C. H. (1989). Rayleigh lidar observations of gravity wave activity in the upper stratosphere at Urbana, Illinois. *J. Atmos. Sci.*, *46*(12), 1838–1854. https://doi.org/10.1175/1520-0469(1989)046<1838:RLOOGW>2.0.CO;2

Gong, S. H., Chen, W. P., Yang, G. T., Guo, J. C., Xu, J. Y., Li, F. Q., Wang, Y. R., Zhang, Y. H., Fu, Y. L., … Cheng, X. W. (2023). Retrieval of temperature structure and identification of gravity wave events in the middle atmosphere from Rayleigh lidar observations. *Acta Opt. Sin. (in Chinese)*, *43*(24), 2428006. https://doi.org/10.3788/AOS230524

Guharay, A., and Sekar, R. (2011). Seasonal characteristics of gravity waves in the middle atmosphere over Gadanki using Rayleigh lidar observations. *J. Atmos. Sol.-Terr. Phys.*, *73*(13), 1762–1770. https://doi.org/10.1016/j.jastp.2011.04.013

Guo, W. J., Yan, Z. A., Hu, X., Guo, S. Y., Song, L., Cheng, Y. Q., and Cui, H. L. (2020). Measuring the three-dimensional structure of gravity waves by Lidar. *Chinese J. Geophys. (in Chinese)*, *63*(2), 394–400. https://doi.org/10.6038/cjg2020M0546

Hauchecorne, A., and Chanin, M. L. (1980). Density and temperature profiles obtained by lidar between 35 and 70 km. *Geophys. Res. Lett.*, *7*(8), 565–568. https://doi.org/10.1029/GL007i008p00565

Hersbach, H., Bell, B., Berrisford, P., Hirahara, S., Horányi, A., Muñoz-Sabater, J., Nicolas, J., Peubey, C., Radu, R., … Thépaut, J. N. (2020). The ERA5 global reanalysis. *Quart. J. Roy. Meteor. Soc.*, *146*(730), 1999–2049. https://doi.org/10.1002/qj.3803

Hu, X., Yan, Z. A., Guo, S. Y., Cheng, Y. Q., and Gong, J. C. (2011). Sodium fluorescence Doppler lidar to measure atmospheric temperature in the mesopause region. *Chin. Sci. Bull.*, *56*(4–5), 417–423. https://doi.org/10.1007/s11434-010-4306-x

Krochin, W., Murk, A., and Stober, G. (2024). Thermal tides in the middle atmosphere at mid-latitudes measured with a ground-based microwave radiometer. *Atmos. Meas. Tech.*, *17*(17), 5015–5028. https://doi.org/10.5194/amt-17-5015-2024

Li, J., Yi, W., Xue, X. H., Lu, M. L., Wang, J. Y., Ye, H. L., and Chen, T. D. (2025). Climatology and long-term trends in middle atmospheric temperatures at mid-latitudes observed by the Rayleigh/Sodium Lidar over Hefei, China (32°N, 117°E). *Earth Planet. Phys.*, *9*(4), 915–924. https://doi.org/10.26464/epp2025045

Llamedo, P., Salvador, J., de la Torre, A., Quiroga, J., Alexander, P., Hierro, R., Schmidt, T., Pazmiño, A., and Quel, E. (2019). 11 years of Rayleigh lidar observations of gravity wave activity above the southern tip of South America. *J. Geophys. Res.: Atmos.*, *124*(2), 451–467. https://doi.org/10.1029/2018JD028673

Wang, Z. J., Chu, X. Z., Huang, W. T., Fong, W., Smith, J. A., and Roberts, B. (2012). Refurbishment and upgrade of Fe Boltzmann/Rayleigh temperature lidar at boulder for a mcmurdo lidar campaign in Antarctica. In *Reviewed and Revised Papers of the 26th International Laser Radar Conference* (pp. 207−210). https://cires1.colorado.edu/science/groups/chu/pubs/documents/ILRC26th_Wang_FeLidarUpgrade.pdf

Xie, F., Wu, D. L., Ao, C. O., and Mannucci, A. J. (2010). Atmospheric diurnal variations observed with GPS radio occultation soundings. *Atmos. Chem. Phys.*, *10*(14), 6889–6899. https://doi.org/10.5194/acp-10-6889-2010

Zhang, R. R., Ji, Y. Z., Xu, X., Lu, Y. X., and Wang, Y. (2024). Impacts of nonhydrostatic orographic gravity wave parameterization on the simulation of atmospheric circulation in climate model. *Chinese J. Geophys. (in Chinese)*, *67*(9), 3277–3289. https://doi.org/10.6038/cjg2024R0545

Zhao, J. (2018). Lidar exploration of a vertical picture of gravity waves in Antarctica from near the surface to the thermosphere [Ph. D. dissertation]. Boulder, Colorado, USA University of Colorado at Boulder.

Zhao, R. C., Dou, X. K., Sun, D. S., Xue, X. H., Zheng, J., Han, Y. L., Chen, T. D., Wang, G. C., and Zhou, Y. J. (2016). Gravity waves observation of wind field in stratosphere based on a Rayleigh Doppler lidar. *Opt. Express*, *24*(6), A581–A591. https://doi.org/10.1364/OE.24.00A581